Supplementary Information to In-Situ Generation of Cu- and Ag-Sn Alloys for CO_2 Reduction from Metal Sulfides

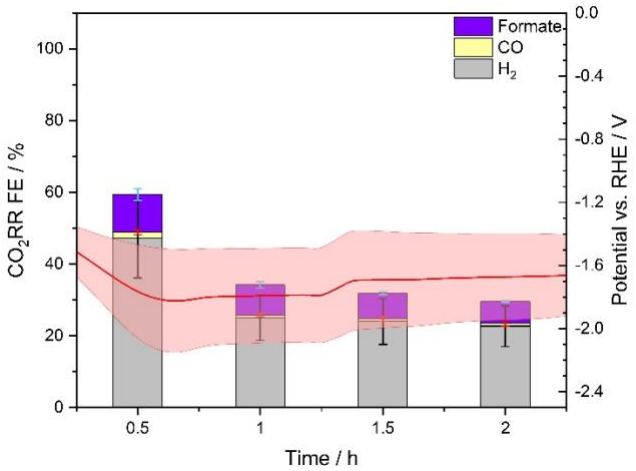

***Figure S1**: CO_2RR on GDE coated with 3mg cm^{-2} Cu_2S and 20 wt. % SustainIon binder. Measurements were conducted in triplicates and standard errors are depicted as ranges at the corresponding FE. The average of the corresponding electrode potentials in V referenced to the RHE are displayed in red, with the standard deviations indicated as shaded areas.*

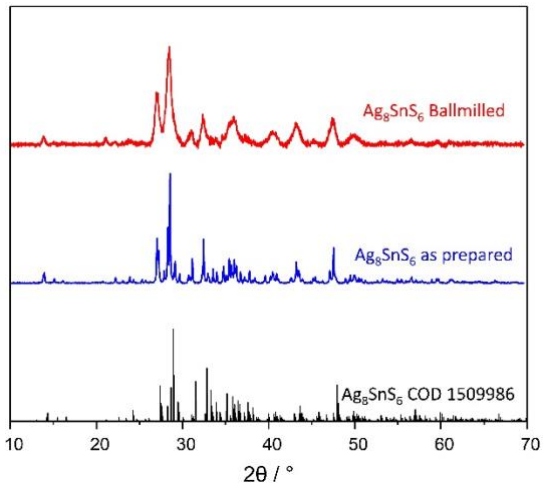

***Figure S2:** PXRD of Ag_8SnS_6 as prepared through high-temperature synthesis at* 900°C for 72h *and the powder ball milled with 5% stearic acid, which was removed by a washing step with ethanol.*

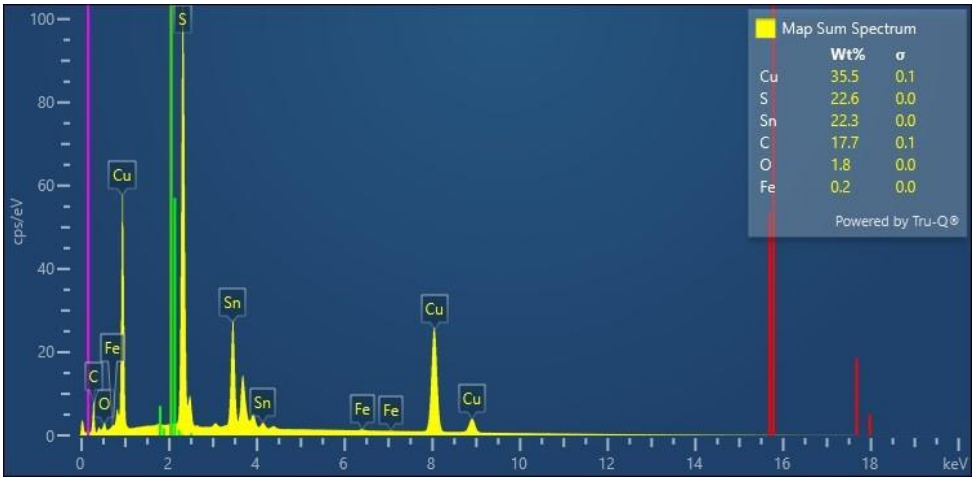

Figure S3: *EDX-Mapping of an as prepared Cu_3SnS_4 gas diffusion electrode* 3.16 : 1.06 : 4.0 for Cu, Sn and S when normalized to the sulfur content..

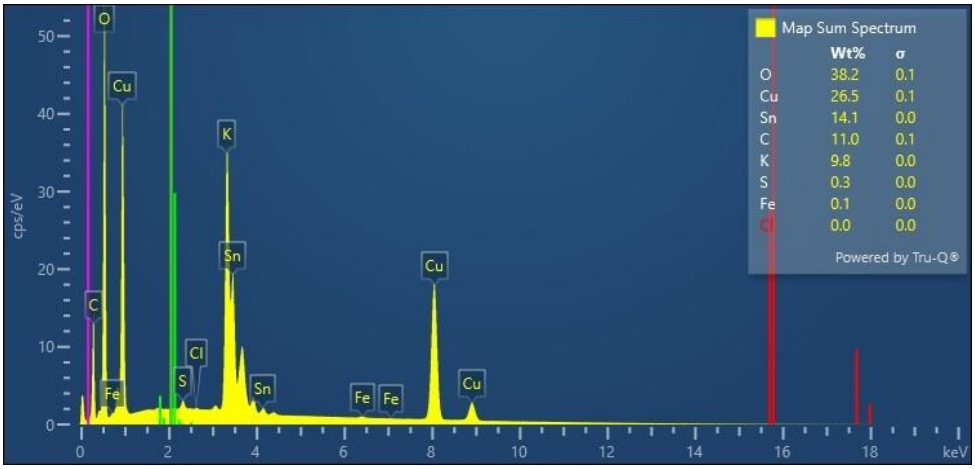

Figure S4*: EDX-Mapping of a Cu_3SnS_4 gas diffusion electrode post electrolysis.*

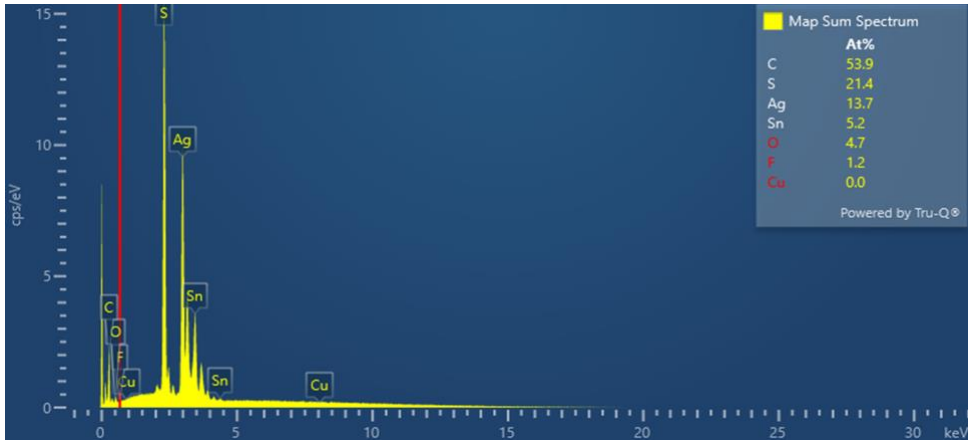

Figure S5: *EDX-Mapping of an as prepared Ag_3SnS_4 gas diffusion electrode with* stoichiometry of $Ag_{2.56}Sn_{0.97}S_4$ (normalized to sulfur).

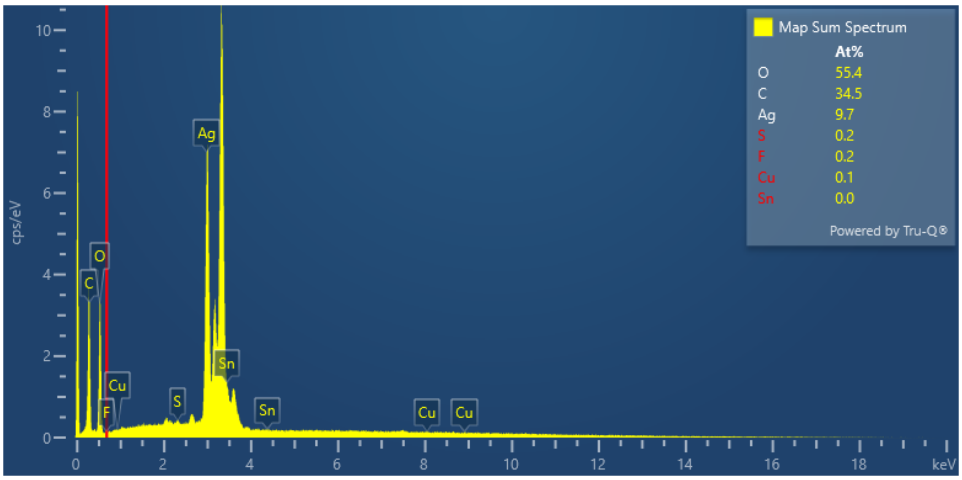

Figure S6: EDX mapping Ag_3SnS_4 gas diffusion electrode surface after electrolysis.

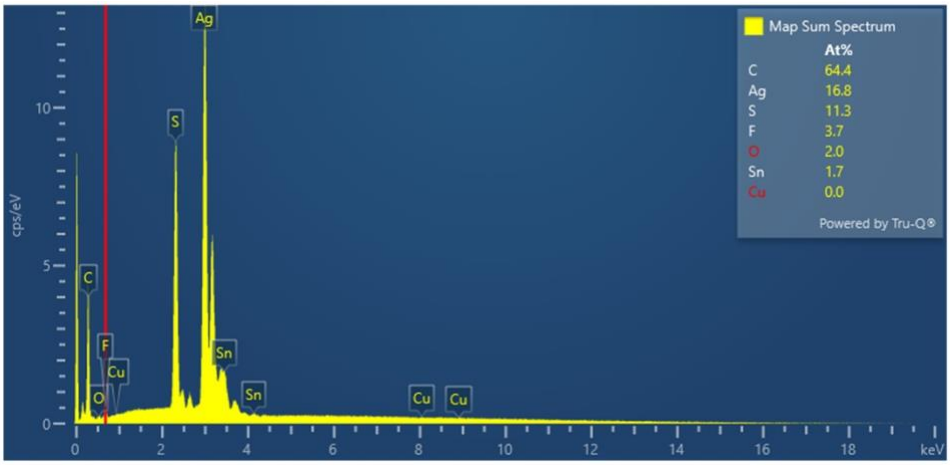

Figure S7: *EDX mapping of* Ag_8SnS_6 gas diffusion electrodes*; normalized to sulfur a stoichiometry of 8.9:0.9:6.0 is found.*

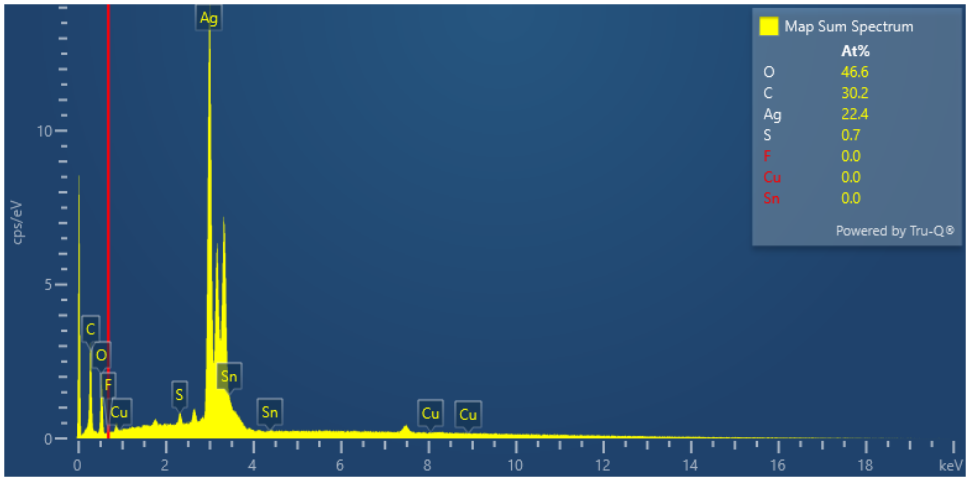

Figure S8: *EDX mapping of* Ag_8SnS_6 gas diffusion electrode surface after electrolysis.

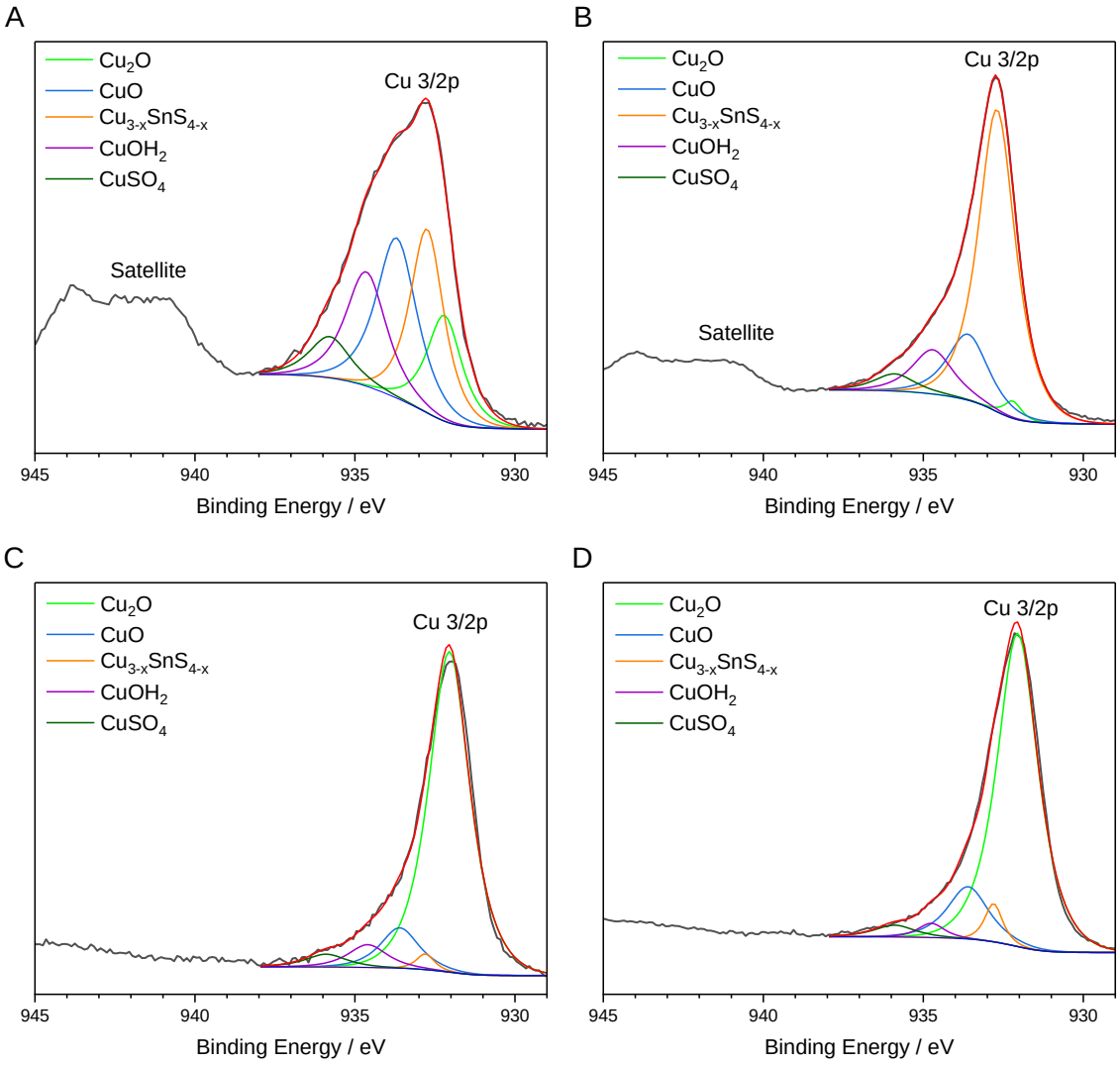

Figure S9: *Cu 2p XPS spectra of an as prepared Cu_3SnS_4 GDE surface (Panel A) and Ar sputtering of the surface layer for 100s (B). Panel C and D show a Cu_3SnS_4 GDE after electrolysis, before and after sputtering of the surface. The sum of fits is displayed in red and the individual peaks were fitted as follows: Cu_2O 932.2 eV (green), Cu_2SnS_3 932.7 eV (orange), CuO 933.7 eV (blue), 934.6 $Cu(OH)_2$ (purple) and 935.8 eV $CuSO_4$ (dark green).*

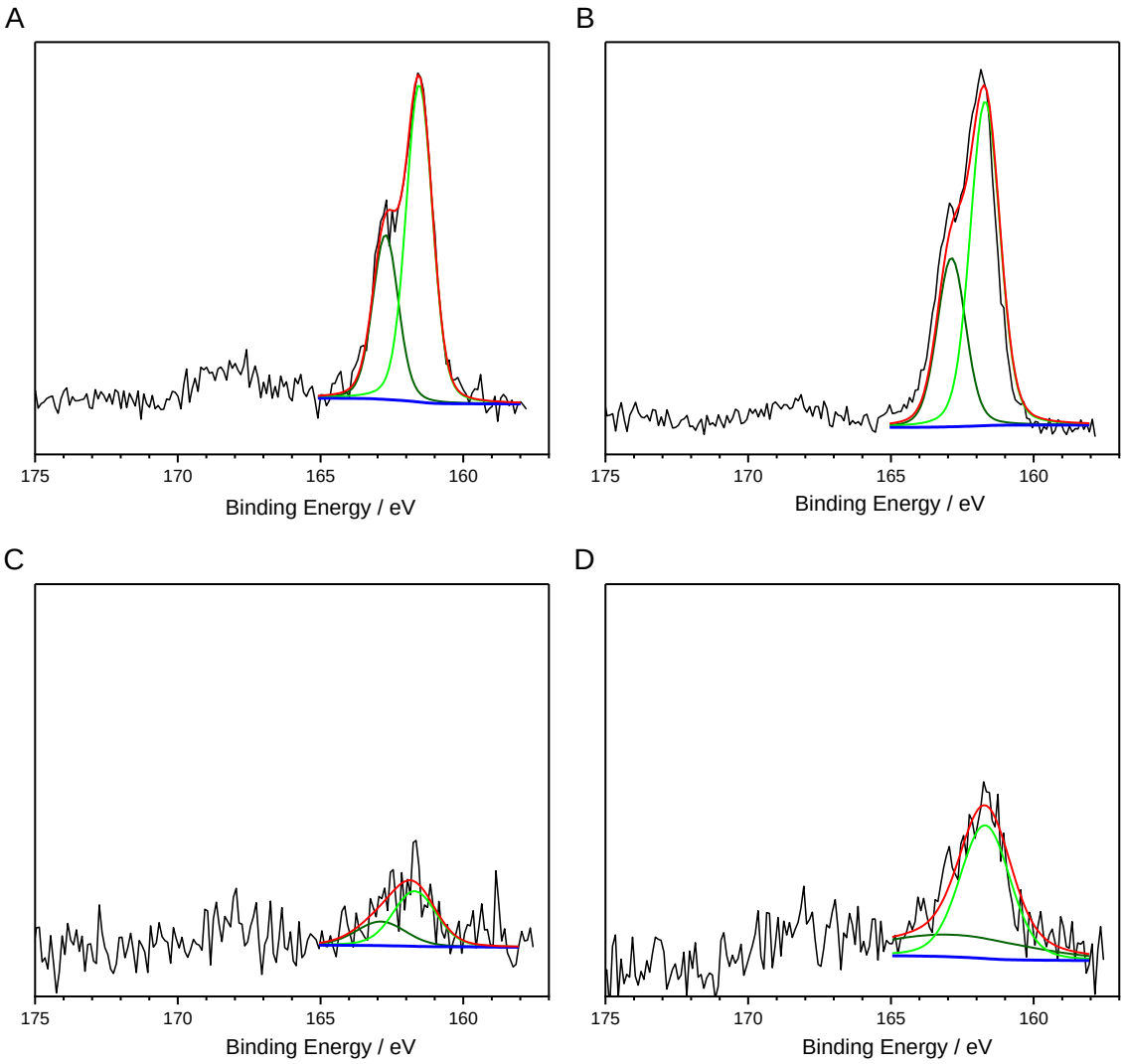

Figure S10: *S 2p XPS spectra of an as prepared Cu_3SnS_4 GDE surface (Panel A) and Ar sputtering of the surface layer for 100s (B). Panel C and D show a Cu_3SnS_4 GDE after electrolysis, before and after sputtering of the surface. The sum of fits is displayed in red and 3/2 and 1/2 metal sulfide signal were observed at 161.7 eV and 162.9 eV respectively.*

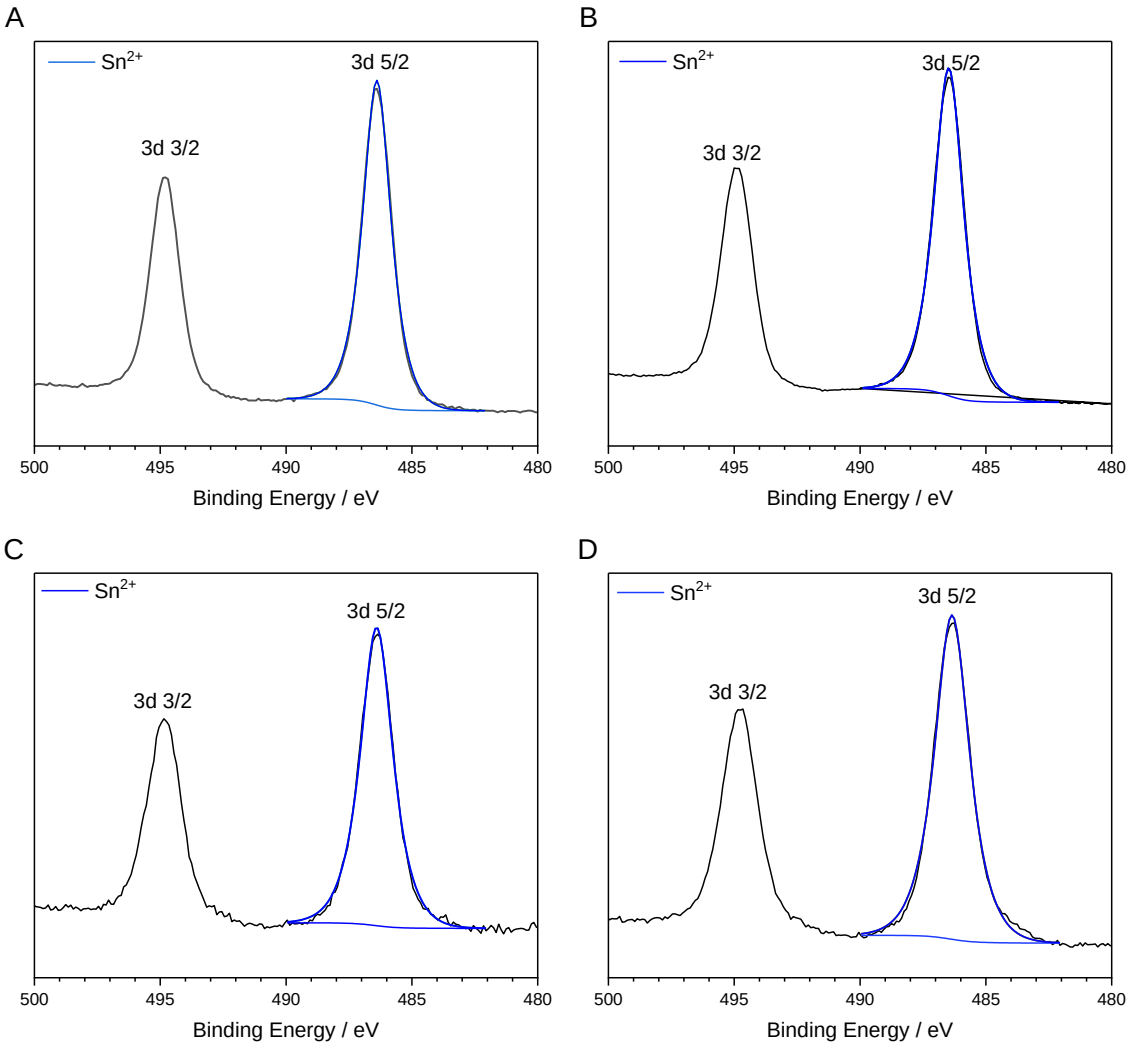

Figure S11: *Sn 3d XPS spectra of an as prepared Cu_3SnS_4 GDE surface (Panel A) and Ar sputtering of the surface layer for 100s (B). Panel C and D show a Cu_3SnS_4 GDE after electrolysis, before and after sputtering of the surface. For both the metal sulfide precursor and the resulting SnO species, signals for the Sn 3d 5/2 transition were recorded at 486.4 eV.*

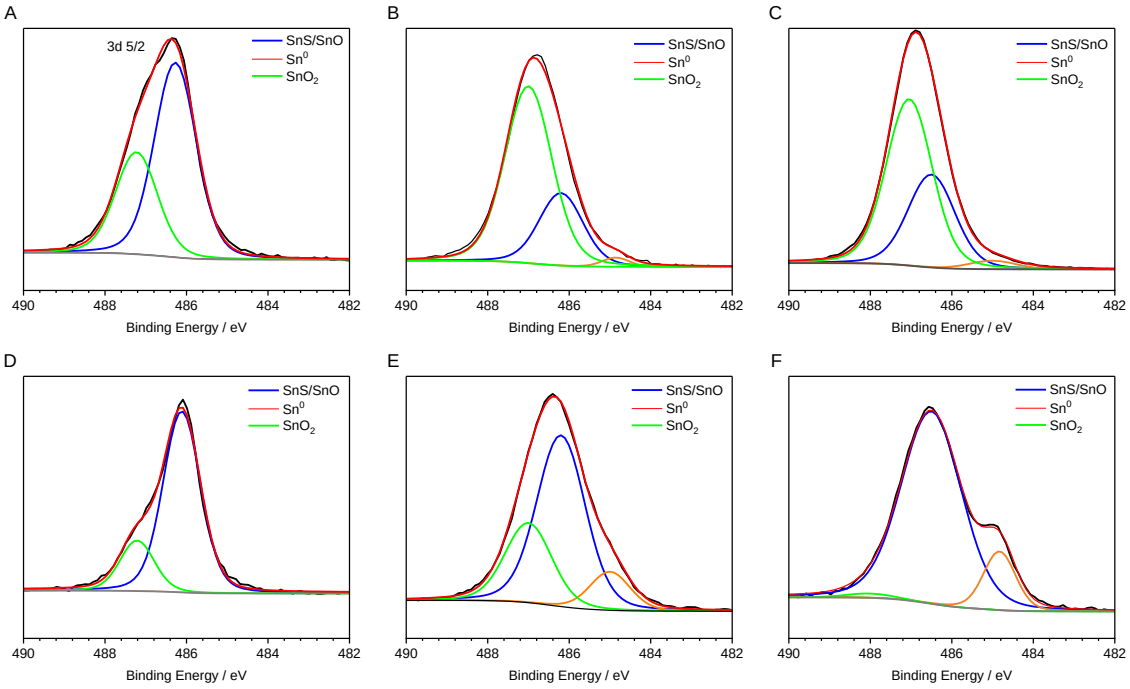

Figure S12: *Sn 3d XPS spectra of an as prepared Ag_3SnS_4 GDE surface (Panel A) and Ar sputtering of the surface layer for 100s (B) after electrolysis for 1h at 100 mA cm^{-2} and 300 mA cm^{-2} each. Panel C corresponds to the Ag_3SnS_4 GDE after electrolysis including a sonication step* in 20 ml HPLC water for 30s, together with Ar sputtering for 100s before analysis. Panel D corresponds to an *Ag_3SnS_4 GDE before and after Ar sputtering, as well as a sonication step for the removal of the top layer before sputtering the electrode surface after electrolysis. The red trace corresponds to the sum of fits, blue to the metal sulfide precursor and the resulting SnO species at 486.4 eV, green to SnO_2 at 487.2 eV and orange to metallic tin at 484.8 eV.*

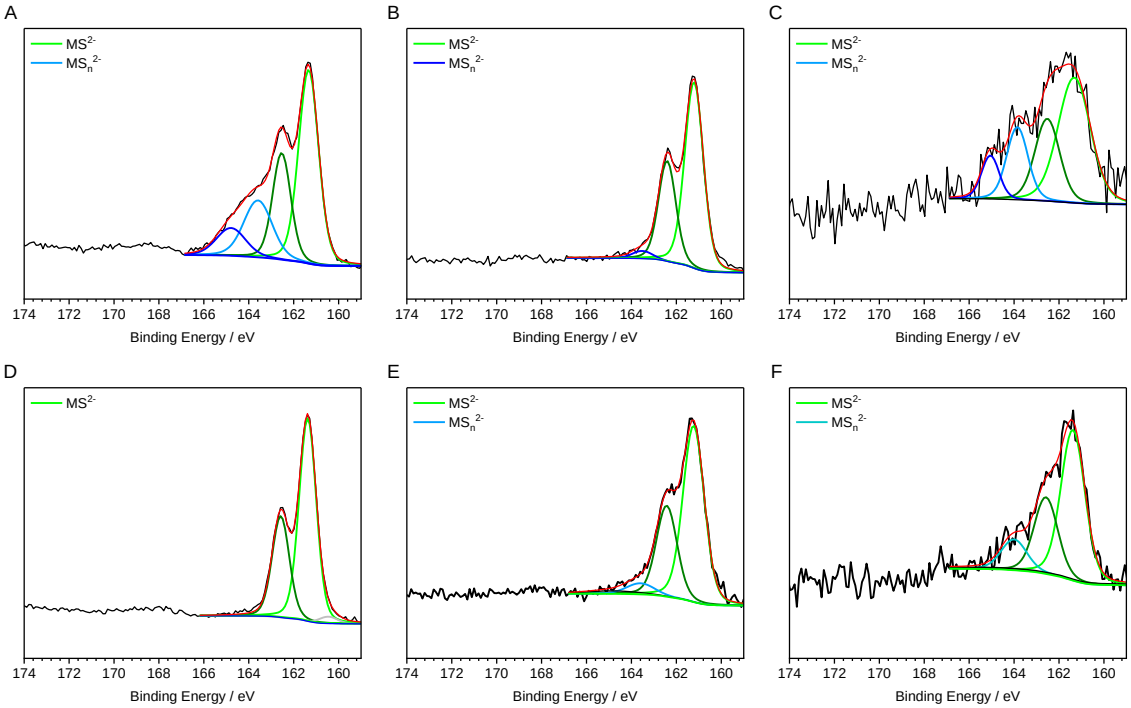

Figure S13: *S 2p XPS spectra of an as prepared Ag_3SnS_4 GDE surface (Panel A) and Ar sputtering of the surface layer for 100s (B) after electrolysis for 1h at 100 mA cm^{-2} and 300 mA cm^{-2} each. Panel C corresponds to the Ag_3SnS_4 GDE after electrolysis including a sonication step* in 20ml HPLC water for 30s, together with Ar sputtering for 100s before analysis. Panel D corresponds to an *Ag_3SnS_4 GDE before and after Ar sputtering, as well as a sonication step for the removal of the top layer before sputtering the electrode surface after electrolysis. The red peak corresponds to the sum of fits, green to the metal sulfide precursor at 161.2 eV, blue to polysulfidic species at 163.6 eV.*

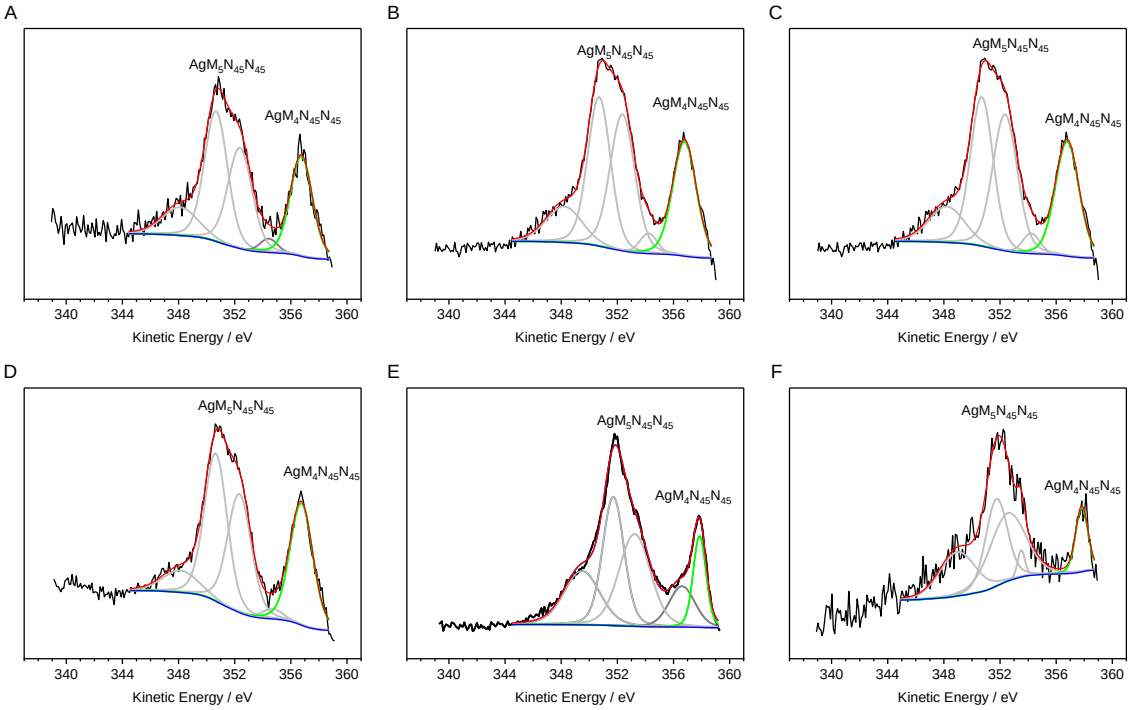

***Figure S14**: Ag MNN Auger transitions of an as prepared Ag_3SnS_4 GDE surface (Panel A), after Ar sputtering of the surface layer for 100s (B), after electrolysis for 1h at 100 mA cm^{-2} and 300 mA cm^{-2} each. Panel C corresponds to the Ag_3SnS_4 GDE after electrolysis including a sonication step* in 20 ml HPLC water for 30s, together with Ar sputtering for 100s before analysis. Panel D corresponds to an *Ag_3SnS_4 GDE before and after Ar sputtering, as well as a sonication step for the removal of the top layer before sputtering the electrode surface after electrolysis. The red peak corresponds to the sum of fits, green to the $M_4N_{4,5}N_{4,5}$ transition used for determination of the Auger parameter together with the Ag 3d 5/2 transition.*

***Table S1.** Ag3d and $AgM_4N_{4,5}N_{4,5}$ peak positions and Auger parameters for Ag_3SnS_4, Ag_8SnS_6 electrodes before and after electrolysis.*

	Ag 3d $_{5/2}$ B.E. / eV	**$AgM_4N_{45}N_{45}$ K.E. / eV**	**Auger parameter**
Ag_3SnS_4	367.0	357.7	724.7
Ag_3SnS_4 *post electrolysis*	367.2	357.7	724.9
Ag_3SnS_4 *post elec., sonicated*	367.1	358.8	725.9
Ag_8SnS_6	367.1	357.6	724.7
Ag_8SnS_6 *post electrolysis*	367.5	358.5	725.5
Ag_8SnS_6 *post elec., sonicated*	367.2	358.9	726.1
Metallic silver	368.8	357.1	725.9
Ag_2S	368.2	356.4	725.6

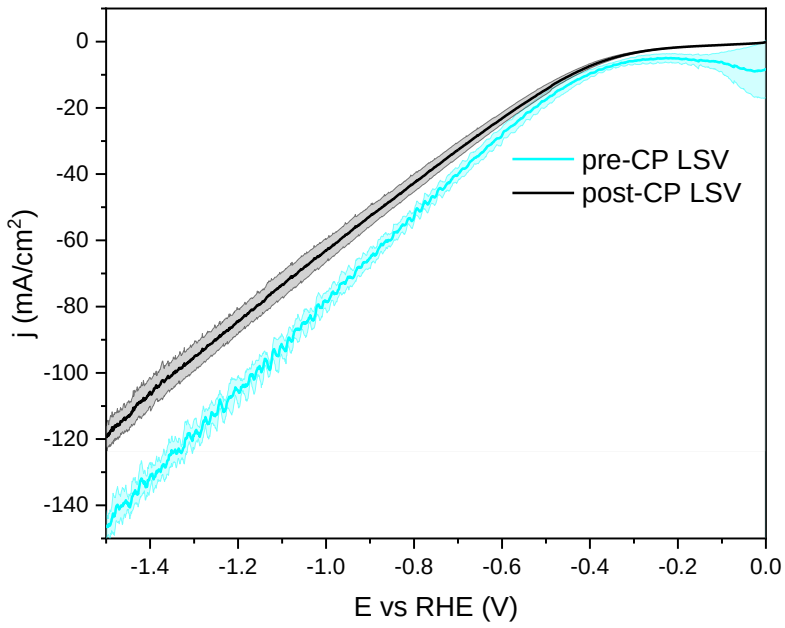

Figure S15. *Linear sweep voltammetry of Cu_3SnS_4 GDE recorded in 1 M KOH with a CO_2 supply of 20 ml min^{-1}. The average of 3 LSV is displayed as a solid line and the standard error is shown as a shaded area, before chronopotentiometry at -100 mA cm^{-2} in teal and after in black. The potentials were recorded using a Gaskatel RHE and are IR corrected based on the measured internal resistance of the electrochemical cell.*

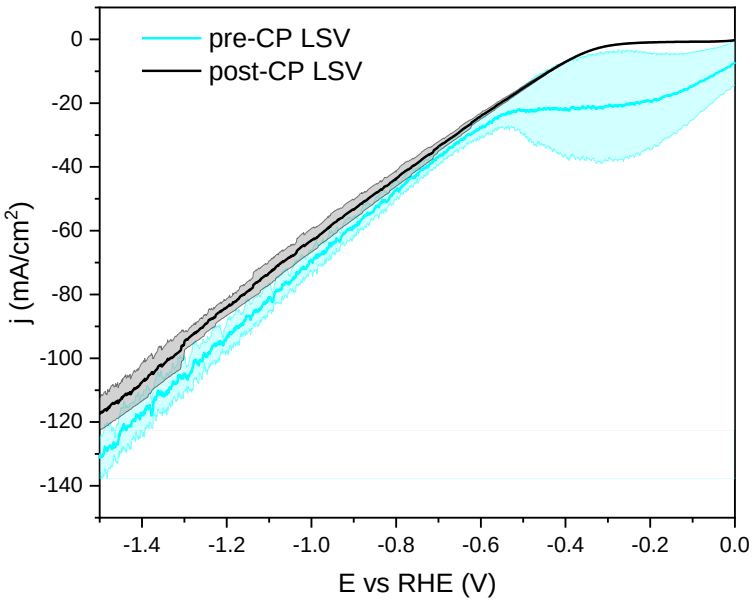

Figure S16. *Linear Sweep Voltammetry of Ag_3SnS_4 GDE recorded in 1 M KOH with a CO_2 supply of 20 ml min^{-1}. The average of 3 LSV is displayed as a solid line and the standard error is shown as a shaded area, before chronopotentiometry at -100 mA cm^{-2} in teal and after in black using IR-corrected electrode potentials.*

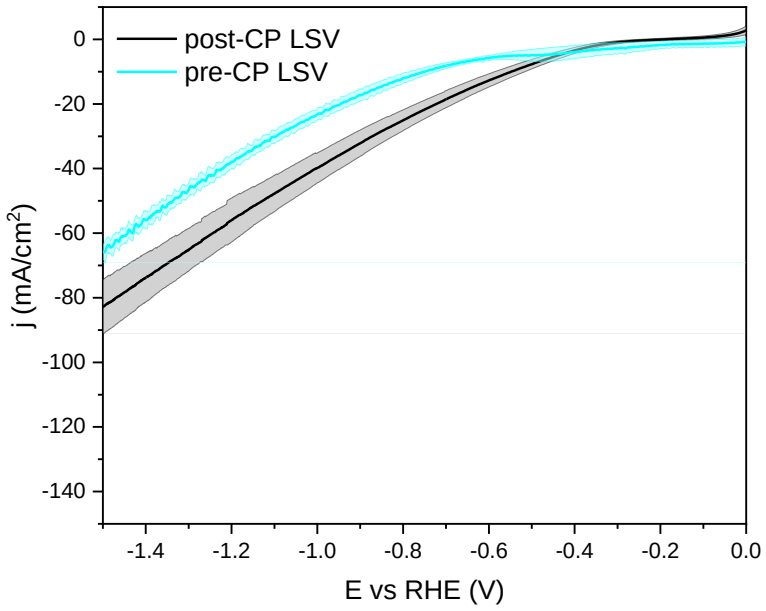

Figure S17. *Linear Sweep Voltammetry of SnS GDE recorded in 1 M KOH with a CO_2 supply of 20 ml min^{-1}. The average of 3 LSV is displayed as a solid line and the standard error is shown as a shaded area, before chronopotentiometry at -100 mA cm^{-2} in teal and after in black using IR-corrected electrode potentials.*

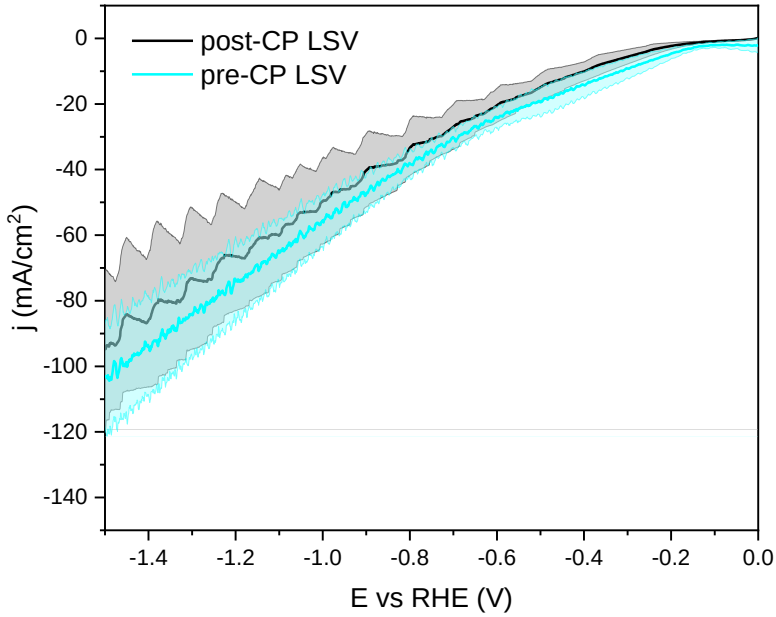

Figure S18. *Linear Sweep Voltammetry of CuS GDE recorded in 1 M KOH with a CO_2 supply of 20 ml min^{-1}. The average of 3 LSV is displayed as a solid line and the standard error is shown as a shaded area, before chronopotentiometry at -100 mA cm^{-2} in teal and after in black using IR-corrected electrode potentials.*

Construction of surface slabs

To explain the electrocatalytic behavior of Ag and Cu, Sn sulfides, a theoretical approach was undertaken. As copper sulfide undergoes an activation under working conditions, the alloying of Cu and Sn is believed to be the main active species in the conversion of CO_2 to formate. (*1*) Thus, supercells and consequently slab models of M_3Sn (M = Ag, Cu), characterized by an orthorhombic Pmmn structure were considered. To describe the enhanced selectivity towards different CO_2RR products, the CO and HCOO molecules were chosen as adsorbates. Additionally, proton adsorption was also considered due to HER being a competing process. The calculations were performed within the DFT formalism using VASP (*2, 3*) code and Perdew-Burke-Ernzerhof (PBE) (*4*) potential with the DFT-D2 method to correct for van der Waals interactions. The plane-wave energy cut-off was set to 520 eV and the k-point mesh were generated using Monkhorst-Pack scheme with distances of 0.025 Å.

The 2x2x2 Me_3Sn supercells were modelled in VESTA software. (*5*) The structures were relaxed using convergence criteria of $1 \cdot 10^{-5}$ eV and $2 \cdot 10^{-2}$ eV/Å^2 for electronic and ionic relaxation, respectively. After the relaxation procedure, the energy of the systems was evaluated again, using stricter electronic convergence criterion of $1 \cdot 10^{-6}$ eV.

Subsequently, slab models of (100), (110) and (010) planes were created with a vacuum level of 15 Å (Fig. S1, Supplementary Information). To assess the stability of the modelled surfaces, the surface energy E_{surf} of the slabs was evaluated using eq. (1):

$$E_{surf} = \frac{E_{slab} - nE_{cell,avg}}{2A}, \quad (1)$$

where E_{slab} – total energy of the slab, $E_{cell,avg}$ – total energy of the supercell divided by the number of atoms in the supercell, n – number of atoms in the slab; A – surface area of the slab, calculated as the product of a and b lattice parameters. Numerical data used in the calculation of surface energies is available in Tables S2-3.

The slabs were again relaxed with two bottom layers of atoms being fixed in the initial positions. The (010) surface was the focus of the investigation due to presence of multiple non-equivalent adsorption sites, as well as lowest surface energy (described in the next section). Placing the adsorbate on the surface resulted in surface coverage of 0.125 ML (1x1). The same numerical parameters and convergence criteria were used as for supercells and pristine slabs, except for systems with OCHO adsorbate for which the ionic convergence criterium was increased to $5 \cdot 10^{-2}$ eV/Å^2. For OCHO, two binding modes were analyzed, namely, *OCHO and *O*OCH. The free-enthalpy change ΔG was calculated using eq. (2):

$$\Delta G = E_{ads} - E_{slab} - E_{molecule} - \Delta E_{ZPE} - T\Delta S, \quad (2)$$

where E_{ads} and E_{slab} – total energies of the systems with and without adsorbates, respectively; $E_{molecule}$ – the calculated energy of either ½H_2, CO, and HCOO molecules; The entropic term $T\Delta S$ was approximated using experimental data for H_2, CO and HCOOH molecules and applying Hess law. ΔE_{ZPE} – difference in zero-point energies taken from VASP and experimental data for gas-phase molecules. Numerical data is available in Table S4.

Surface energy

The surface energies of (010), (100) and (110) Me_3Sn planes are presented in Figure S19. For both Cu- and Ag-based alloys, the same trends are observable: the (010) plane is the most stable, the (100) plane is the least stable, and the (110) plane exhibits intermediate values of E_{surf}. However, in all cases, Ag-rich systems exhibit lower plane energies, suggesting greater thermodynamic stability. Incorporating Cu into the structure raises this energy by about 30%, likely due to the mismatch of ionic radii of respective elements. The presence of 4d electrons causes Ag ions to have larger radii in every coordination compared to Cu ions [6]. This also affects the crystallographic cell parameters and volumes. The volume of the Ag-based alloy is 30% higher than that of Cu-based one, which correlates with the higher surface energies. Higher surface energy typically indicates greater surface tension and a higher degree of disorder, leading to increased chemical reactivity. This, in turn, means that for catalytic reactions requiring active sites with higher energy, planes with higher surface energy will be more effective. Thus, the system will need less energy from external sources to drive the reduction reactions. In other words, the ΔG of adsorption should be more spontaneous on Cu_3Sn as opposed to Ag_3Sn.

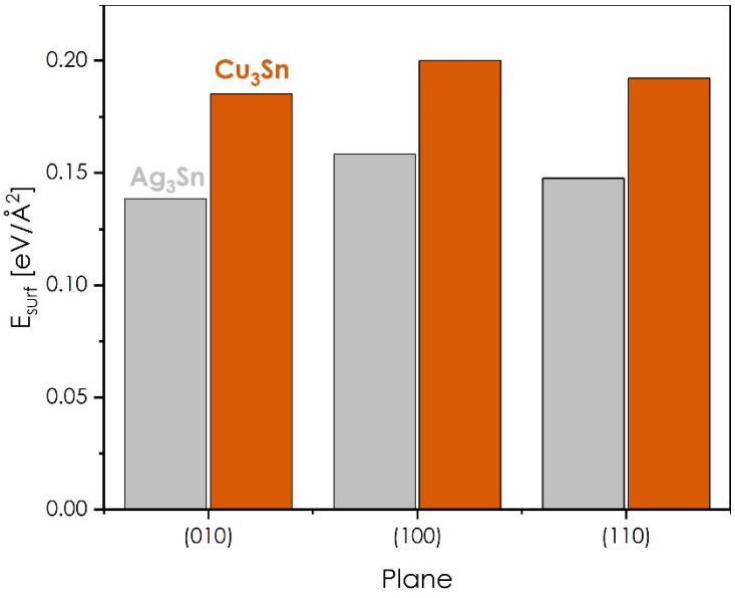

***Fig S19**. Surface energy of different M_3Sn planes.*

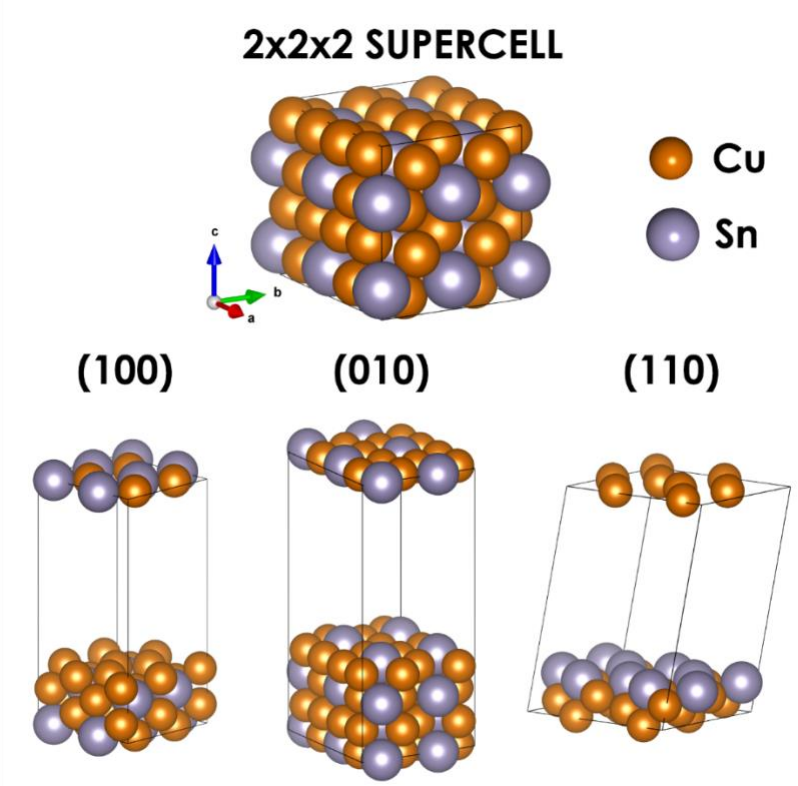

Fig S20. *The Cu_3Sn supercell and slab models of (100), (010), (110) planes.*

Table S2. *Unit cell parameters of 2x2x2 M_3Sn supercells (M = Ag, Cu).*

Lattice parameter	Ag_3Sn	Cu_3Sn
$\boldsymbol{a}$ [Å]	12.123	11.012
$\boldsymbol{b}$ [Å]	9.541	8.470
$\boldsymbol{c}$ [Å]	10.626	9.647
$\boldsymbol{\alpha = \beta = \gamma}$ [°]	90	
$\boldsymbol{V}$ [Å^3]	1229.092	899.742

Table S3. *Total energies, surface areas and surface energies of pristine Me_3Sn supercells and slabs.*

Model	Number of atoms in the cell	E_{DFT} [eV]	A [Å^2]	E_{surf} [eV/Å^2]
		Ag_3Sn		
2x2x2 supercell	64	-229.37	-	-
(010) slab	64	-211.52	128.91	0.138
(100) slab	32	-98.64	101.38	0.158
(110) slab	32	-90.49	164.00	0.148
		Cu_3Sn		
2x2x2 supercell	64	-268.95	-	-
(010) slab	64	-249.29	106.23	0.185
(100) slab	32	-118.13	81.71	0.200
(110) slab	32	-108.72	134.02	0.192

Table S4. *Binding (interactions) lengths, total energies, zero-point energies, adsorption energies and free-enthalpy change for different adsorption sites on Me_3Sn slab models. r_i correspond to the distance between the adsorbate and individual atoms.*

	r_1 [Å]	r_2 [Å]	r_3 [Å]	E_{DFT} [eV]	E_{ZPE} [eV]	TS [eV]	ΔG [eV]
H							
*Ag	1.65			-214.166	0.101	0.000	0.775
'Ag'Ag'Ag	1.91	1.91	1.92	-214.922	0.146	0.009	0.055
'Ag'Ag	1.81	1.81		-214.791	0.126	0.003	0.172
'Ag'Ag (Sn)	1.90	1.90	2.17	-214.663	0.124	0.016	0.285
*Sn	1.77			-214.124	0.123	0.061	0.778
*Ag (110)	1.81	2.31	2.54	-93.2494	0.093	0.010	0.637
*Cu	1.52			-252.218	0.108	0.000	0.495
'Cu'Cu (Sn)	1.66	1.67	2.38	-252.271	0.140	0.024	0.451
'Cu'Cu'Cu	1.74	1.74	1.80	-252.993	0.167	0.006	-0.227
'Cu'Cu (SnSn)	1.67	1.67		-252.494	0.159	0.017	0.254
'Cu'Sn	1.60	2.07		-252.285	0.125	0.004	0.441
*Sn	1.76			-251.841	0.127	0.053	0.838
*Cu (110)	1.62	2.39	2.38	-111.590	0.078	0.000	0.528
CO and OC							
*Ag (OC)	3.20			-226.371	0.135	0.057	0.402
*Ag (Sn)	2.11	3.50		-226.727	0.166	0.146	-0.013
'Ag'Ag'Ag	2.38	2.30	2.30	-226.645	0.161	0.176	0.034
'Ag'Ag	2.26	2.26		-226.680	0.169	0.178	0.005
*Cu	1.86			-264.934	0.188	0.104	-0.391
'Cu'Cu	1.98	1.98		-265.093	0.178	0.160	-0.616
'Cu'Cu (SnSn)	2.01	2.01		-264.672	0.174	0.157	-0.196
*Sn	3.41			-264.165	0.143	0.231	0.207
OCHO and OOCH							
'Ag'Ag'Ag	2.35	2.36	2.36	-237.858	0.590	0.253	-2.238
'Ag'Ag	2.29	2.27		-237.810	0.586	0.270	-2.211
*Ag*Sn	2.29	2.24		-238.163	0.605	0.227	-2.501
**Sn	2.34	2.41		-237.857	0.595	0.274	-2.253
**Cu	2.07	2.71		-275.618	0.582	0.218	-2.255
*Cu*Cu	2.00	2.01		-276.274	0.609	0.203	-2.869
*Cu'Cu'Cu	2.05	2.18	2.18	-276.247	0.617	0.196	-2.824
'Cu'Cu'Cu	2.17	2.16	2.17	-275.872	0.584	0.192	-2.481
'Cu'Cu (Sn)	2.17	2.17	2.42	-275.422	0.585	0.255	-2.093
*Cu*Sn	2.02	2.28		-275.949	0.612	0.209	-2.547

	r_1 [Å]	r_2 [Å]	r_3 [Å]	E_{DFT} [eV]	E_{ZPE} [eV]	TS [eV]	ΔG [eV]
**Sn	2.51	2.30		-275.363	0.589	0.211	-1.986
Gas-phase molecules							
½ H_2				-3.386	0.273	0.205	
HCOO				-23.917	0.528	0.555	
CO				-14.776	0.216	0.611	

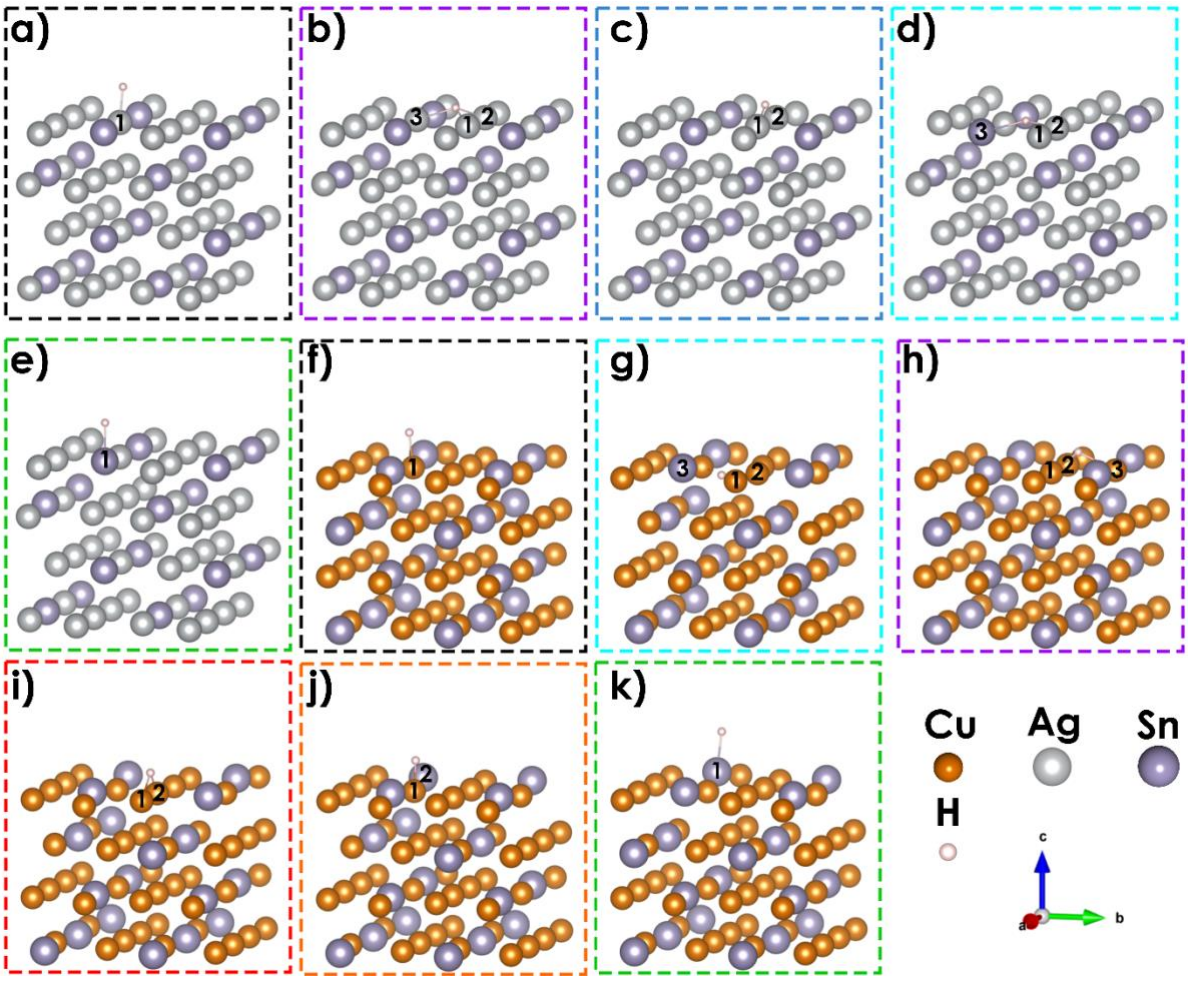

Fig S21. **H sites on (010) Me_3Sn planes after the final relaxation process:* ***a)*** **Ag;* ***b)*** *'Ag'Ag'Ag;* ***c)*** *'Ag'Ag';* ***d)*** *'Ag'Ag (Sn);* ***e)*** **Sn;* ***f)*** **Cu;* ***g)*** *'Cu'Cu (Sn);* ***h)*** *'Cu'Cu'Cu;* ***i)*** *'Cu'Cu (SnSn);* ***j)*** *'Cu'Sn;* ***k)*** **Sn. The numbers correspond to the atom in the site and r_i in Table S4.*

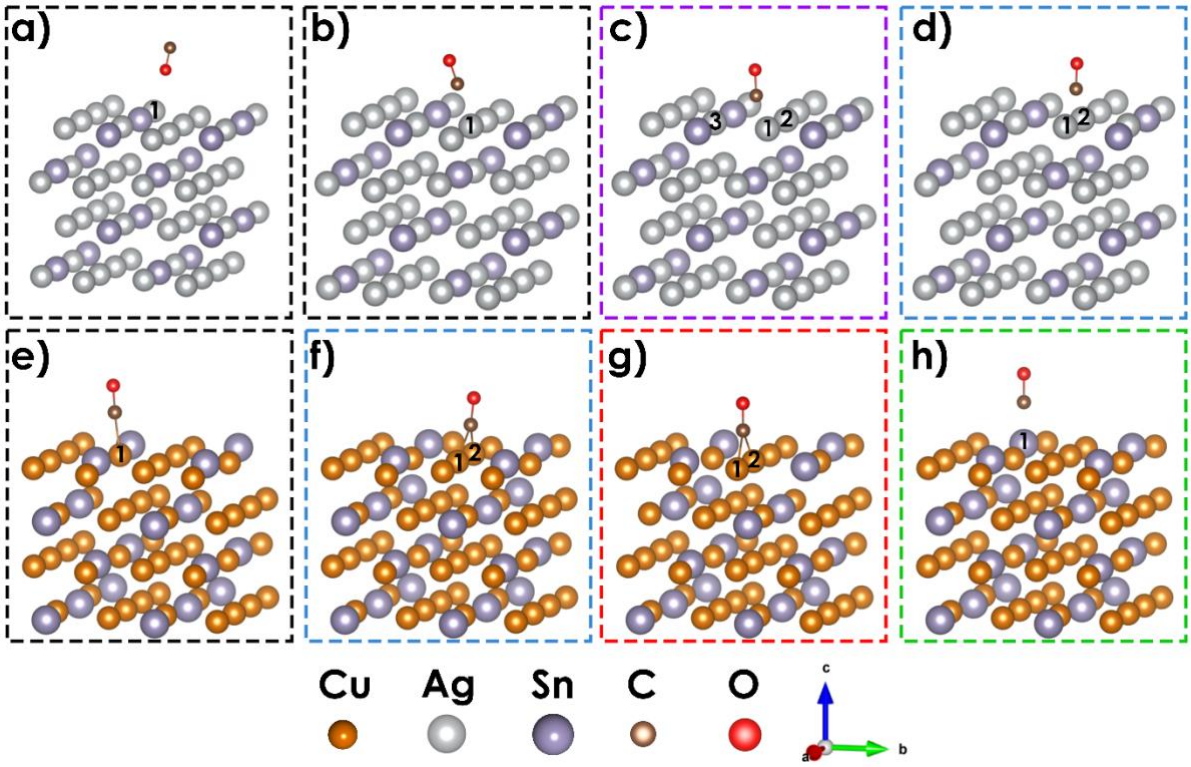

Fig S22. **CO sites on (010) Me_3Sn planes after the final relaxation process:* ***a)*** **Ag (OC);* ***b)*** **Ag* ***c)*** *'Ag'Ag'Ag';* ***d)*** *'Ag'Ag;* ***e)*** **Cu;* ***f)*** **'Cu'Cu;* ***g)*** *'Cu'Cu (SnSn);* ***h)*** **Sn. The numbers correspond to the atom in the site and r_i in Table S4.*

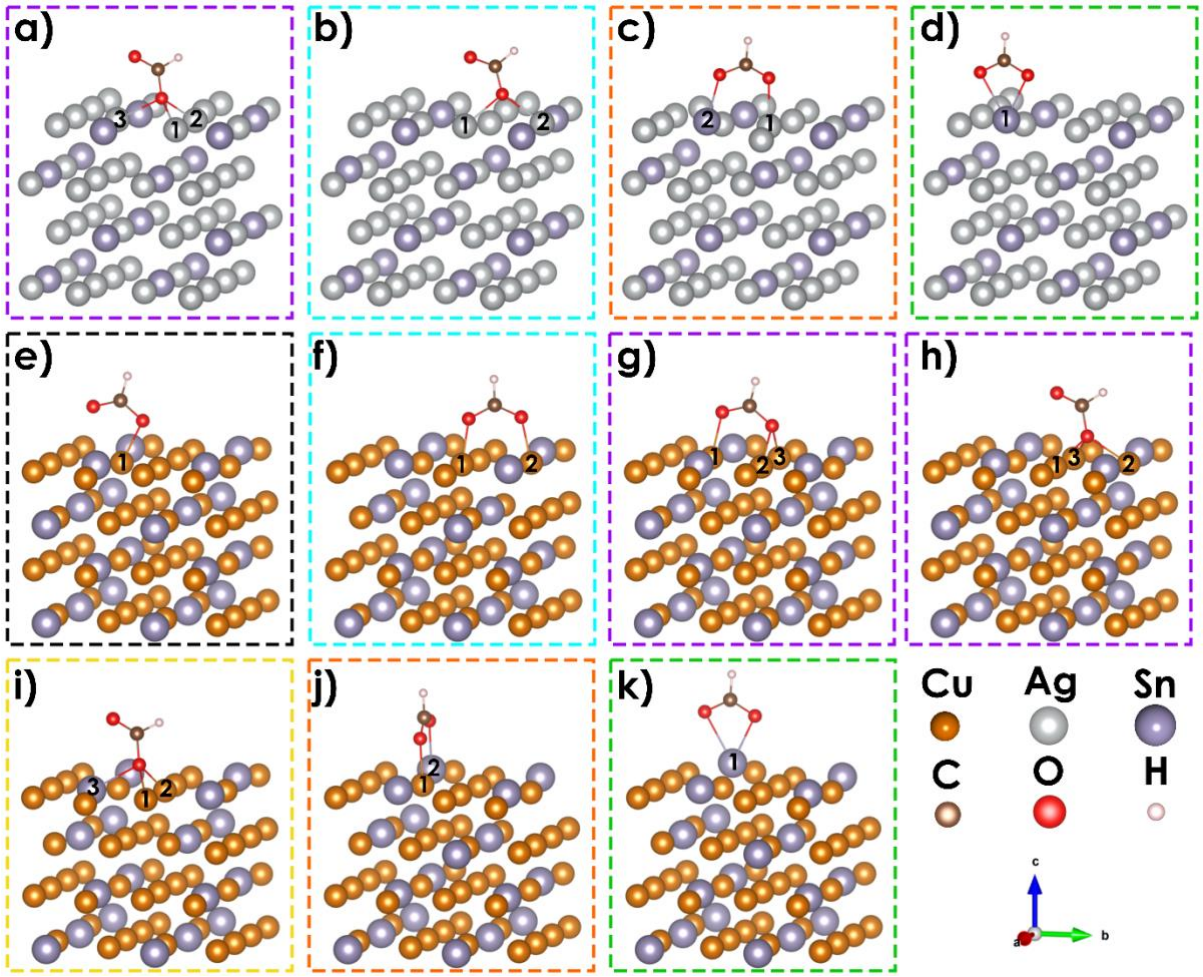

Fig S23. **OCHO and *O*OCH sites on (010) Me_3Sn planes after final relaxation process:* ***a)*** *'Ag'Ag'Ag;* ***b)*** *'Ag'Ag (Sn);* ***c)*** **Ag*Sn;* ***d)*** ***Sn;* ***e)*** ***Cu;* ***f)*** **Cu*Cu (Sn);* ***g)*** **Cu'Cu'Cu;* ***h)*** *'Cu'Cu'Cu;* ***i)*** *'Cu'Cu (Sn);* ***j)*** **Cu*Sn;* ***k)*** ***Sn. The numbers correspond to the atom in the site and r_i in Table S4.*

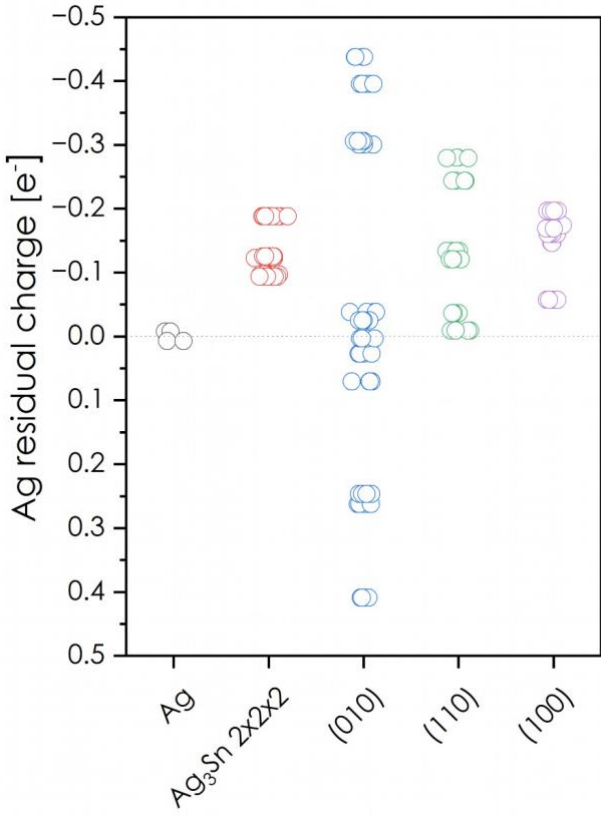

Fig S24. *Distribution of the computed Ag residual Bader charge in Ag, Ag_3Sn supercell, (010), (110) and (100) facets of Ag_3Sn. Each dot represents an atom in the respective model using the above-described optimized geometries.*

Table S5 *Comparison of CO_2RR activity in respect to HCOOH production of this work and published catalysts in literature.*

Cell type	*Catalyst*	*Electrolyte*	*Potential vs. RHE (V)*	*FE (%)*	*J_{HCOOH} (mA cm^{-2})*	*Reference*
Flow Cell	*Ag_3SnS_4*	*1M KOH*	*-1.1*	*54*	*162*	*This work*
Flow Cell	*Cu_3SnS_4*	*1M KOH*	*-1.0*	*57*	*57*	*This work*
Flow cell	*Cu_2Sn_S*	*0.5 M $KHCO_3$*	*-2.2*	*96*	*241*	*(1)*
H-type cell	*Ag_3Sn / SnO_2*	*0.5 M $NaHCO_3$*	*-0.8*	*87*	*25*	*(6)*
H-type cell	*Pd_4Ag*	*0.1 M $KHCO_3$*	*-0.2*	*100.0*	*2.1*	*(7)*
H-type cell	*N-SnO_2*	*0.1 M $KHCO_3$*	*-1.2*	*89.1*	*15.5*	*(8)*
H-type cell	*3 at.% Cu-SnS_2*	*0.5 M $KHCO_3$*	*-1.0*	*90.9*	*23.8*	*(9)*
Flow cell	*S-Bi-NSs*	*1 M KOH*	*-0.9*	*96*	*192*	*(10)*
Flow-cell	*SnS*	*1 M KOH*	*-1.0*	*97.4*	*88.6*	*(11)*

References

1. Li, K.; Xu, J.; Zheng, T.; Yuan, Y.; Liu, S.; Shen, C.; Jiang, T.; Sun, J.; Liu, Z.; Xu, Y.; Chuai, M.; Xia, C.; Chen, W. In Situ Dynamic Construction of a Copper Tin Sulfide Catalyst for High-Performance Electrochemical CO 2 Conversion to Formate. *ACS Catal.* **2022,** *12* (16), 9922–9932. DOI: 10.1021/acscatal.2c02627.
2. Kresse, G.; Furthmüller, J. Efficiency of ab-initio total energy calculations for metals and semiconductors using a plane-wave basis set. *Computational Materials Science* **1996,** *6* (1), 15–50. DOI: 10.1016/0927-0256(96)00008-0.
3. Kresse, G.; Hafner, J. Ab initio molecular dynamics for liquid metals. *Physical review. B, Condensed matter* **1993,** *47* (1), 558–561. DOI: 10.1103/PhysRevB.47.558.
4. Perdew, J. P.; Burke, K.; Ernzerhof, M. Generalized Gradient Approximation Made Simple. *Phys. Rev. Lett.* **1996,** *77* (18), 3865–3868. DOI: 10.1103/PhysRevLett.77.3865.
5. Momma, K.; Izumi, F. VESTA 3 for three-dimensional visualization of crystal, volumetric and morphology data. *J Appl Cryst* **2011,** *44* (6), 1272–1276. DOI: 10.1107/S0021889811038970.
6. Luc, W.; Collins, C.; Wang, S.; Xin, H.; He, K.; Kang, Y.; Jiao, F. Ag-Sn Bimetallic Catalyst with a Core-Shell Structure for CO2 Reduction. *Journal of the American Chemical Society* **2017,** *139* (5), 1885–1893. DOI: 10.1021/jacs.6b10435.
7. Han, N.; Sun, M.; Zhou, Y.; Xu, J.; Cheng, C.; Zhou, R.; Zhang, L.; Luo, J.; Huang, B.; Li, Y. Alloyed Palladium-Silver Nanowires Enabling Ultrastable Carbon Dioxide Reduction to Formate. *Advanced Materials* **2021,** *33* (4), e2005821. DOI: 10.1002/adma.202005821.

8. Li, Z.; Cao, A.; Zheng, Q.; Fu, Y.; Wang, T.; Arul, K. T.; Chen, J.-L.; Yang, B.; Adli, N. M.; Lei, L.; Dong, C.-L.; Xiao, J.; Wu, G.; Hou, Y. Elucidation of the Synergistic Effect of Dopants and Vacancies on Promoted Selectivity for CO2 Electroreduction to Formate. *Advanced Materials* **2021,** *33* (2), e2005113. DOI: 10.1002/adma.202005113.

9. Chen, M.; Wan, S.; Zhong, L.; Liu, D.; Yang, H.; Li, C.; Huang, Z.; Liu, C.; Chen, J.; Pan, H.; Li, D.-S.; Li, S.; Yan, Q.; Liu, B. Dynamic Restructuring of Cu-Doped SnS2 Nanoflowers for Highly Selective Electrochemical CO2 Reduction to Formate. *Angewandte Chemie (International ed. in English)* **2021,** *60* (50), 26233–26237. DOI: 10.1002/anie.202111905.

10. Peng, C.-J.; Zeng, G.; Ma, D.-D.; Cao, C.; Zhou, S.; Wu, X.-T.; Zhu, Q.-L. Hydrangea-like Superstructured Micro/Nanoreactor of Topotactically Converted Ultrathin Bismuth Nanosheets for Highly Active CO2 Electroreduction to Formate. *ACS applied materials & interfaces* **2021,** *13* (17), 20589–20597. DOI: 10.1021/acsami.1c03871.

11. Zou, J.; Lee, C.-Y.; Wallace, G. G. Boosting Formate Production from CO2 at High Current Densities Over a Wide Electrochemical Potential Window on a SnS Catalyst. *Advanced science (Weinheim, Baden-Wurttemberg, Germany)* **2021,** *8* (15), e2004521. DOI: 10.1002/advs.202004521.